

## Line emission mapper microcalorimeter spectrometer

Simon R. Bandler,<sup>a,\*</sup> Joseph S. Adams,<sup>a,b</sup> Edward G. Amatucci,<sup>b,a</sup>  
Edgar R. Canavan,<sup>a</sup> James A. Chervenak,<sup>a</sup> Renata S. Cumbee,<sup>a</sup>  
Johannes P. D. Dercksen,<sup>b,c</sup> Michael J. DiPirro,<sup>b,a</sup> William B. Doriese,<sup>b,d</sup>  
Megan E. Eckart,<sup>b,e</sup> Manuel Gonzalez,<sup>b,f</sup> Janice Houston,<sup>g</sup> Brian Jackson,<sup>c</sup>  
Amir E. Jahromi,<sup>a</sup> Steven J. Kenyon,<sup>a</sup> Caroline A. Kilbourne,<sup>b,a</sup>  
Edmund Hodges-Kluck,<sup>a</sup> Ralph Kraft,<sup>b,g</sup> Xiaoyi Li,<sup>a</sup> Maxim Markevitch,<sup>a</sup>  
Dan McCammon,<sup>b,h</sup> Jeffrey R. Olson,<sup>b,i</sup> Elizabeth Osborne,<sup>b,i</sup> Kazuhiro Sakai,<sup>b,a,b</sup>  
Daniel Patnaude,<sup>g</sup> Frederick S. Porter,<sup>b,a</sup> Damien Prêle,<sup>b,f</sup>  
Peter J. Shirron,<sup>b,a</sup> Stephen J. Smith,<sup>b,a</sup> Terrence M. Smith,<sup>a</sup>  
Nicholas A. Wakeham,<sup>b,a,b</sup> and Henk J. van Weers<sup>c</sup>

<sup>a</sup>NASA - Goddard Space Flight Center, Greenbelt, Maryland, United States

<sup>b</sup>CRESST and University of Maryland, Baltimore County, Maryland, United States

<sup>c</sup>SRON, Netherlands Institute for Space Research, Leiden, The Netherlands

<sup>d</sup>National Institute of Standards and Technology, Boulder, Colorado, United States

<sup>e</sup>Lawrence Livermore National Laboratory, Livermore, California, United States

<sup>f</sup>Astroparticle and Cosmology Laboratory, Paris, France

<sup>g</sup>Smithsonian Astrophysical Observatory, Cambridge, Maryland, United States

<sup>h</sup>University of Wisconsin, Madison, Wisconsin, United States

<sup>i</sup>Lockheed Martin Space, Palo Alto, California, United States

**ABSTRACT.** The line emission mapper (LEM) is a probe-class mission concept that is designed to detect x-ray emission lines from hot ionized gas ( $T > 10^6$  K) that will enable us to test galaxy evolution theories. It will permit us to study the effects of stellar and black-hole feedback and flows of baryonic matter into and out of galaxies. The key to being able to study the hot gases that are otherwise invisible to current imaging x-ray spectrometers is that the energy resolution is sufficient to use cosmological redshift to separate extragalactic source lines from foreground Milky Way emission. LEM incorporates a large-format microcalorimeter array instrument called the LEM microcalorimeter spectrometer (LMS) with a light-weight x-ray optic with 10" half power diameter angular resolution. The LMS microcalorimeter array has pixels with 15" pixel pitch over a 33' field of view (FOV) optimized for the 0.3 to 2 keV energy band. The central 7' region of the array has an energy resolution of 1.3 eV at 1 keV and the rest of the FOV has 2.5 eV energy resolution at 1 keV. The array will be read out with state-of-the-art time-division multiplexing. We present an overview of the LMS instrument, including details of the entire detection chain, the focal plane assembly, as well as the cooling system and overall mechanical and thermal design. For each of the key technologies, we discuss the current technology readiness level and the plan to advance them to be ready for flight. We also describe the current system design and our estimate for the mass, power, and data rate of the instrument. The design details presented concentrate primarily on the unique aspects of the LMS design compared with prior missions and confirm that the type of microcalorimeter instrument needed for LEM is not only feasible but also technically mature.

© The Authors. Published by SPIE under a Creative Commons Attribution 4.0 International License. Distribution or reproduction of this work in whole or in part requires full attribution of the original publication, including its DOI. [DOI: [10.1117/1.JATIS.9.4.041002](https://doi.org/10.1117/1.JATIS.9.4.041002)]

**Keywords:** microcalorimeter; spectrometer; x-ray; cryogenics; detector; astrophysics

\*Address all correspondence Simon R. Bandler, [Simon.R.Bandler@nasa.gov](mailto:Simon.R.Bandler@nasa.gov)

## 1 Introduction

The line emission mapper (LEM) astrophysics probe<sup>1</sup> will fill in a major missing puzzle piece in our understanding of cosmic ecosystems<sup>2</sup> by charting flows of mass and energy in and around galaxies. LEM will do this by mapping important x-ray emission lines from hot ionized gas ( $T > 10^6$  K) that encode the temperature, chemical abundances, mass, and velocity needed to develop galaxy evolution theories. We already know that diffuse hot gas plays an essential role in a galaxy's life: enormous reservoirs of hot gas around and between galaxies provide the fuel for future growth,<sup>3–6</sup> whereas their metal and entropy content trace the “feedback” from stars, supernovae, and supermassive black holes that regulate galaxy growth.<sup>7,8</sup> Within galaxies, the hot interstellar medium acts as a galactic cytoplasm by transporting metals, energy, and magnetic fields, mediating communication between different parts of the galaxy and pressurizing the neutral medium.<sup>9–11</sup> In regions of active star formation, flows of supernova-heated hot gas<sup>12–16</sup> can both trigger star formation and destroy stellar nurseries.<sup>17,18</sup>

Yet studies of interstellar, circumgalactic, and intergalactic hot gas are beset by order-of-magnitude uncertainties in mass, metallicity, velocity, and even luminosity because this gas is diffuse, very faint, and observed through a forest of much brighter foreground emission lines. These characteristics strongly limit studies with current or planned instruments. Silicon-based x-ray imaging spectrometers (e.g., on board Chandra, XMM-Newton, Suzaku, or eROSITA) can make high angular resolution maps but lack the energy resolution to separate source emission from foregrounds and backgrounds or to measure Doppler broadening of the lines. Meanwhile, x-ray grating spectrometers (Chandra LETG, XMM-Newton RGS) have the energy resolution but cannot observe faint, extended sources. The LEM microcalorimeter spectrometer (LMS) solves these problems via high-resolution ( $<2.5$  eV) non-dispersive imaging spectroscopy [15" pixels over a 30 arcmin field of view (FOV)] in the 0.3 to 2 keV band. A key advantage of LMS over current imaging spectrometers is that the energy resolution is sufficient to use cosmological redshift to separate extragalactic source lines from foreground Milky Way emission; for important oxygen and iron lines, this will reduce the background by up to a factor of 50. Hence, LMS enables accurately mapping temperature, density, metal content, and velocities in individual supernova remnants, massive star clusters, the hot interstellar medium, the circumgalactic and intracluster medium, and the cosmic web. These measurements will tell us how mass, energy, and metals flow from sources to sinks over an enormous range of distance scales, from 10 to  $10^7$  light years.

The LMS is paired with an x-ray optic with 10" angular resolution and large effective area. The 10" half power diameter resolution ensures that almost all x-rays from coincident point sources (often much brighter than the diffuse gas) are contained within 1 to 2 LMS pixels (15" or 290  $\mu\text{m}$  pitch at the 4-m telescope focal length), whereas the product of high effective area and FOV (grasp) enables LEM to map very extended objects at moderate angular resolution in a reasonable amount of time. As such, LEM will not only transform our understanding of dilute million-degree gas but will be a powerful general-purpose x-ray workhorse observatory in the 2030s.

The LMS microcalorimeter array has a 33' FOV. The central 7' region of the array consists of  $\sim 800$  transition-edge sensors (TESs), optimized for the 0.3 to 2 keV bandpass, with an energy resolution of 1.3 eV at 1 keV. The rest of the FOV is covered by 4-pixel TES hydras with 2.5 eV energy resolution at 1 keV,<sup>19</sup> as depicted in Fig. 1. The LMS instrument requirements are summarized in Table 1 below.

The overall design of the LMS that meets all of these requirements is shown in Fig. 2. The x-rays are reflected from the 4-m focal length x-ray optic, pass through a magnetic diverter (MD) and infrared blocking filters (BFs), and then focused onto the LMS detectors inside the focal plane assembly (FPA). The detectors are microcalorimeters in which the sensor is a superconducting metal, voltage-biased in-between its superconducting and normal states such that any small change in temperature, causes a relatively large change in current passing through it.

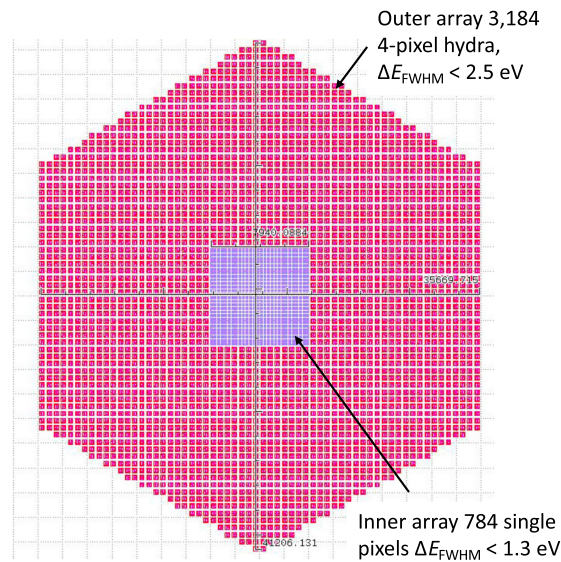


**Fig. 1** Layout of the LMS focal plane array. The (blue) inner 7' consists of single 15'' pixels with <math><1.3\text{ eV}</math> energy resolution, and the outer array consists of 4-pixel hydras, where each pink square represents a 4-pixel hydra with pixel with <math><2.5\text{ eV}</math> energy resolution.

**Table 1** The LMS instrument requirements.

LEM instrument requirements				
	Energy (KeV)	0.5	1	1.5
Effective area (on axis)	cm <sup>2</sup>	1200	1850	1400
FOV (diameter)		30 arcmin		
Angular resolution		18 arcsec		
Energy resolution		2.5 eV (1.3 eV)		
Energy band		0.2 to 2 keV		
Background level	Maximum background count rate of 2 counts/s/(30 arcmin × 30 arcmin)/keV			
Energy scale knowledge		0.25 eV relative/1 eV absolute		

These changes in current are proportional to the energy of the x-rays, which are measured with very high precision using a superconducting quantum interference device (SQUID).

The MD that is installed around the x-ray beam path is there to minimize the number of background charged particles that are incident on the focal plane. These charged particles (chiefly protons and electrons) are naturally present in the LEM environment and would produce an important background and noise source if they were incident on the x-ray detector. The MD efficiently deflects this contribution outside of the region of the detector without affecting the x-ray throughput. The baseline MD design is based on a similar application for the Athena x-ray integral field unit (X-IFU) and WFI instruments, which uses a Hallbach design comprised of N42H grade BREMAG NdFeB magnets.<sup>20</sup> The LEM MD consists of a ring of magnets with a 38 cm inner diameter placed  $\sim 1$  m from the detector. In between the MD and the LMS cryostat, there is a filter wheel that will be described in Sec. 6. After the x-rays pass through an opening in the LMS cryostat, they pass through the cryostat aperture assembly, which will be described in Sec. 6 and into the FPA (described in Sec. 2). The outer part of the FPA is at 4 K, and inside are the microcalorimeter detector array, a cryogenic anti-coincidence detector, and cold multiplexed SQUIDs that are used to read out the microcalorimeters (described in Secs. 3 and 4). These are all cooled to 40 mK.

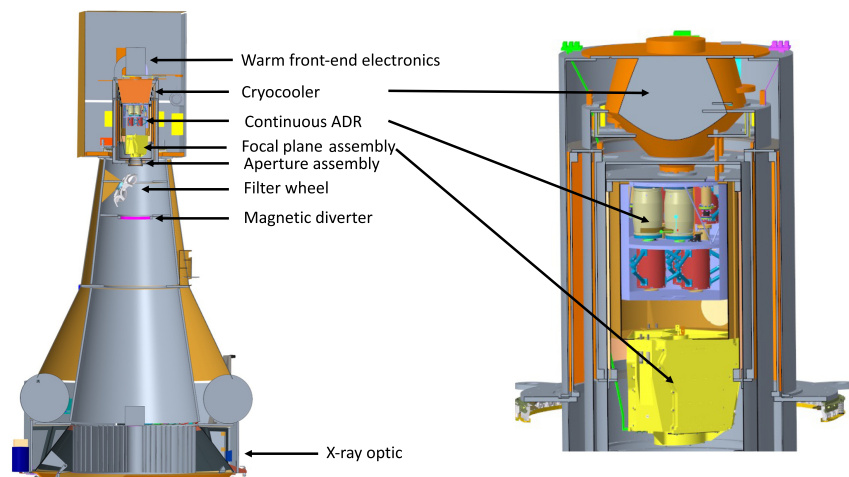


**Fig. 2** Layout of the LMS within the LEM telescope. The left image shows a cross-section of the whole LEM telescope in which the LMS is embedded. The right image shows a magnified view of the region of the LMS cryostat. In this figure, the FPA is not sectioned.

A cold harness (not shown) runs between the FPA and warm front-end electronics (WFEEs) located at the top of the cryostat that mostly consists of the low noise amplifiers (LNAs) of the differential signals from the SQUID read-out channels. These signals are then sent to the digital electronics and event processor (DEEP) that are electronics boxes directly attached to radiators surrounding the cryostat and shown in yellow in Fig. 2. The warm electronics is described in Sec. 5. The cooling of the system from room temperature down to the microcalorimeter temperature of 40 mK is achieved through the combination of a single (mature) 4-stage pulse tube cryocooler to cool to a temperature 4.0 K<sup>21</sup> and then a continuous adiabatic demagnetization refrigerator (CADR) that provides continuous cooling at 350 and 40 mK, as summarized in Sec. 7.

Section 8 summarizes the overall thermal system design and in Sec. 9 we summarize the instrument mass, power, and data rate, and discuss the implications of the chosen design on cost. In Sec. 10, we summarize the plans to evolve the technical readiness of all parts of the LMS to a NASA technical readiness level (TRL) of TRL-6.

The whole LEM telescope design has a lot of heritage from the Japanese XRISM mission<sup>22</sup> and earlier incarnations of that telescope, which were Hitomi,<sup>23</sup> Suzaku,<sup>24</sup> and Astro-E. These missions were developed as a collaboration between JAXA and NASA as the major mission partners, with key NASA contributions coming from LEM team members being the microcalorimeter, its FPA, and its silicon junction-gate field-effect transistor based read-out, as well the three-stage ADR. The LMS read-out chain has direct heritage from the two flights of the Micro-X sounding rocket.<sup>25</sup> Although no meaningful astrophysics data were possible from the first flight due to an avionics failure, the flight successfully demonstrated in space the operation of a microcalorimeter array using TES microcalorimeters, read out using SQUID time-division multiplexing (TDM) for the first time, similar to the type of detectors and readout that the LMS will use. The detectors and TDM read-out survived the flight without issues, and calibration x-rays were successfully read-out during the flight. The second flight was successful and considered flawless, and the data collected are still being analyzed.

The x-ray integral field unit (X-IFU) microcalorimeter instrument, to be flown on ESA's flagship mission called Athena, has been in development for more than 7 years.<sup>22</sup> This development has added a lot of maturity to the design of the LMS detection chain architecture with many members of the LMS team participating in this mission. Although optimized for very different x-ray astrophysics observations and thus for a very different x-ray energy range with different performance characteristics, the basic TESs being used in the microcalorimeter array, the TDM multiplexing, and the room temperature electronics are very similar. In addition to spaceflight, TES microcalorimeters and TDM read-out as x-ray and gamma-ray spectrometers have now been deployed in a broad range of terrestrial applications.<sup>26-34</sup>

## 2 Focal Plane Assembly

The FPA contains the LEM's cryogenic detector array and its cold TDM readout electronics and it provides the mechanical support, the thermal isolation and the electromagnetic shielding required to operate the sensor array at  $T_0 \leq 40$  mK inside of the instrument cryostat. The LMS FPA design is largely based upon Athena X-IFU FPA design<sup>35</sup> and the prior SPICA-Safari FPA concept,<sup>36</sup> scaled in size and aperture diameter to accommodate the large FOV of the LMS. The overall scaling of the FPA as compared to the X-IFU FPA is well understood. The necessary design work has already taken place to ensure that the magnetic shielding is sufficient, the higher mass can be suspended with a sufficiently high eigenfrequency, and the conductive heat loads through the different temperature stages have been calculated and found to be low enough to be handled by the CADR with plenty of margin.

Table 2 summarizes the conceptual mass and thermal budgets of the pre-phase-A conceptual design, whereas Fig. 3 is a cut-away view of the preliminary conceptual design. The heart of the FPA is the  $T_0$  detector assembly, as shown in Fig. 4, which integrates the main sensor array with its time-division multiplexed first-stage SQUID amplifiers, plus the anti-coincidence detector (anti-co) detector mounted in close proximity to the main sensor.

**Table 2** Key FPA technical properties.

Mass	$m_{T_0} = 2.35$ kg, $m_{T_1} = 1.35$ kg, and $m_{T_2} = 6.8$ kg (all CBE values) total: 10.5 kg
Volume (CBE)	$H = 285$ mm excl. thermal strap and 4-K baffle $D = 330$ mm, excl. 4-K harness connector interface
Temperature levels	$T_0 = 40$ mK, $T_1 = 350$ mK, and $T_2 = 4.0$ K
Heat-loads	$P_{T_0} = 875$ nW, $P_{T_1} = 84$ $\mu$ W, $P_{T_2} = 0.3$ mW, excl. 2 $\times$ thermal margin
Magnetic shielding	$\sim 30\times$ attenuation versus static field present at cooldown $>1000\times$ attenuation versus time-varying field during operation
Stiffness	First eigenfrequency $\sim 235$ Hz
Strength	Design limit load $<40$ g for 10.5 kg mass

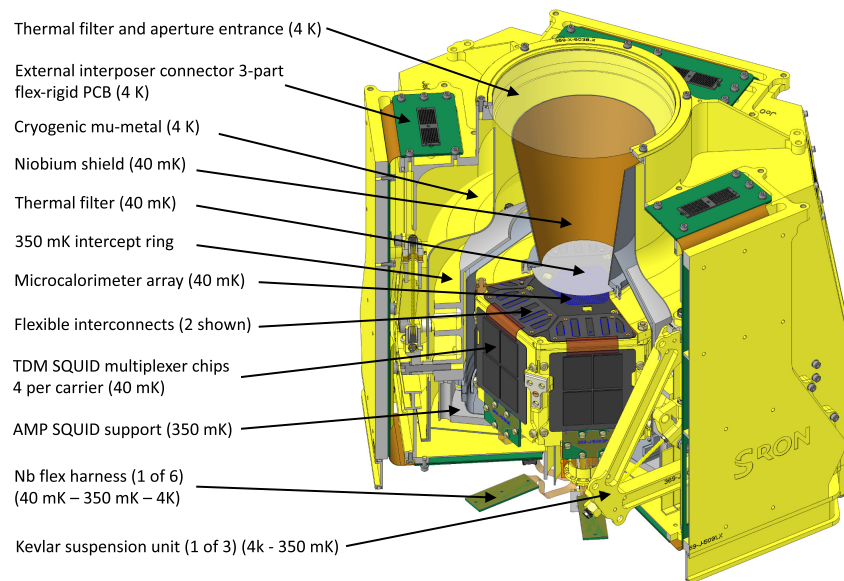


**Fig. 3** A cut-away view of the LEM FPA with the hexagonal 40 mK detector assembly visible inside the nested 40 mK Nb shield, 350 mK heat-sink ring, 4.0 K CMM shield, and 4.0 K mechanical housing.

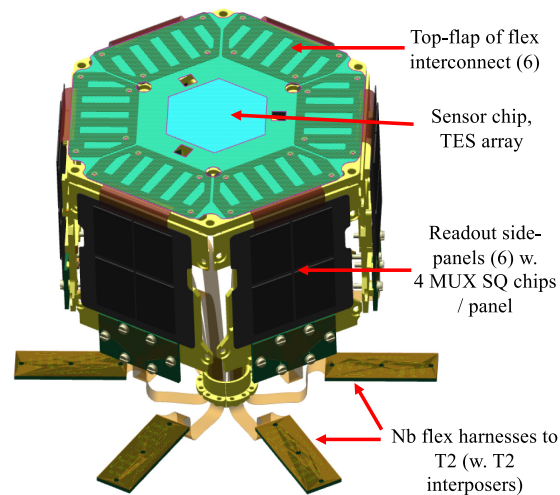


**Fig. 4** Mechanical model of the hexagonal 40 mK ( $T_0$ ) stage. The hexagonal detector wafer sensor array on the front surface, epoxied to an array of leaf springs (flexures) that absorb any mismatch in the coefficient of thermal expansion while maintaining a stable position. Wirebonds are made from the detector wafer to six flaps of corner-turning flex on which two-layer Nb wiring connects to the six panels of multiplexed cold read-out, using TDM. A thermal strap connects this stage to the CADR.

The large-format sensor array is mounted on an array of leaf springs (flexures) to absorb differential thermal expansion between the Si chip and Cu structure and maintain alignment during cooldown. Superconducting flex ribbon cables connect the sensor array with the TDM multiplexer chips, which are mounted on six readout panels on the sides of the hexagonal  $T_0$  structure.

The coldest stage of the FPA at  $T_0 = 40$  mK is thermally isolated from the cryocooler cold tip and the warmest outer stage shield of the FPA at  $T_2 = 4.0$  K by a two-layer Kevlar suspension with an intermediate steady mechanical temperature stage  $T_1 = 350$  mK, as shown in Fig. 5(a). Each suspension stage combines three suspension sub-assemblies formed by three Kevlar cords. A SQUID assembly is mounted on the bottom of the  $T_1$  ring that houses the part of the detection chain to be described in Sec. 4, which are the amp SQUIDs. A high-density superconducting Nb flex harness connects the detector stage ( $T_0$ ) to the AMP SQUID stage ( $T_1$ ) and then continues to connect to large flex-PCBs at the  $T_2$  stage. These PCBs contain

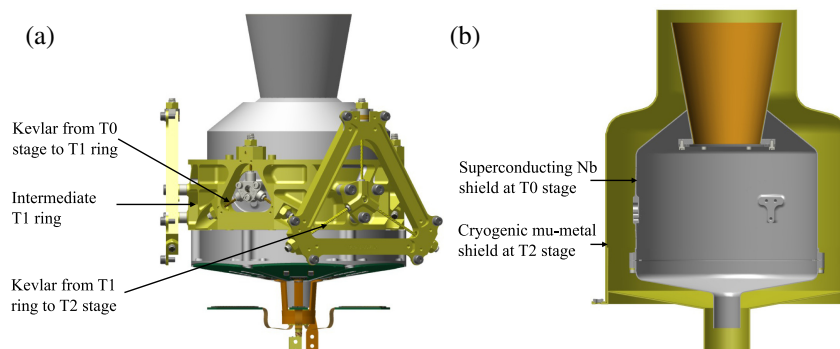


**Fig. 5** (a) The two-layer Kevlar suspension that suspends the 40 mK  $T_0$  stage from the 4.0 K  $T_2$  stage with an intermediate  $T_1$  ring nominally at 350 mK. Each three-cord Kevlar sub-assembly constrains 2 degrees of freedom, with three assemblies combining to realize a stiff strong suspension that ensures the stability of the position of the  $T_0$  stage relative to  $T_2$  after thermal cycling. (b) The two-layer magnetic shield applied in the LEM FPA, with a superconducting Nb shield at the  $T_0$  stage and a CMM shield at the  $T_2$  stage (separated by the  $T_1$  ring of the thermal suspension, not shown in this cut-away view).

resistive bias divider circuits and filters for signal conditioning in the detection chain readout circuit. In addition, the PCBs provide a connectorized termination for the dewar cold harness in the form of mating pads for interposer-style connectors.

Within the FPA, the detector is shielded by a combination of a superconducting Nb magnetic shield at  $T_0$  and a cryogenic mu-metal (CMM) shield at  $T_2$ . At the x-ray entrance aperture, there are only thermal infrared filters placed at both  $T_0$  and  $T_2$ . These filters primarily only block IR radiation and otherwise provide some electromagnetic shielding. Figure 5(b) is a cut-away view of the combined Nb and CMM shields. The large-format LEM detector array and its large viewing angle to the x-ray optic require a relatively “open” entrance aperture in the magnetic shields, which limit the achievable shielding effectiveness. FEM analysis has been demonstrated to be able to accurately predict the observed magnetic shielding that is achievable from this sort of arrangement, as shown in Fig. 6(b) for the shields shown in Fig. 6(a).<sup>37</sup> FEM analysis of the LMS baseline magnetic shielding geometry predicts a shielding effectiveness of the CMM shield alone of at least a factor of 30, with the limiting case being for an axial external field. This is sufficient to ensure that the field trapped into the Nb shield at cooldown remains less than  $2 \mu\text{T}$  for external fields of up to  $60 \mu\text{T}$ . At operating temperature, the CMM and Nb shield combine to provide a higher shielding effectiveness, with the limiting case being for a lateral field that bends into the conical opening, yielding vertical field components at the edges of the sensor array. In this configuration, as shown in Fig. 6(c), the shielding effectiveness, expressed as the magnitude of the lateral external field to the vertical component of the field at the detector array,

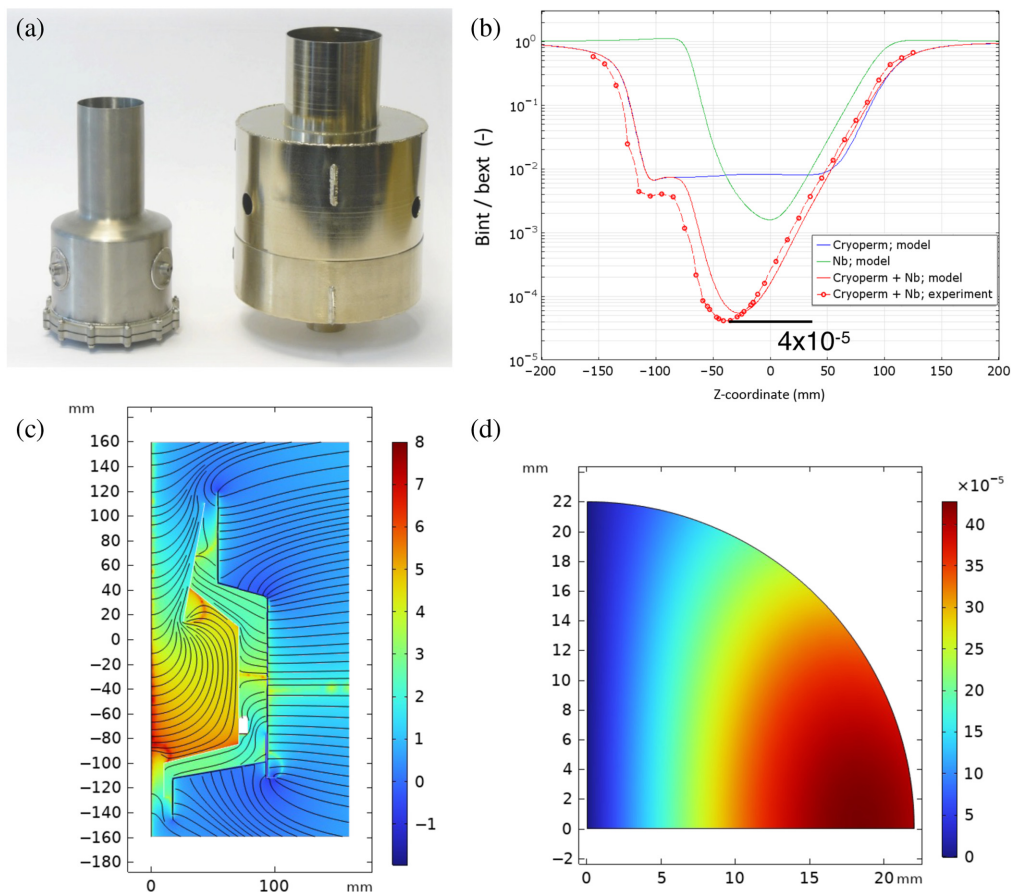


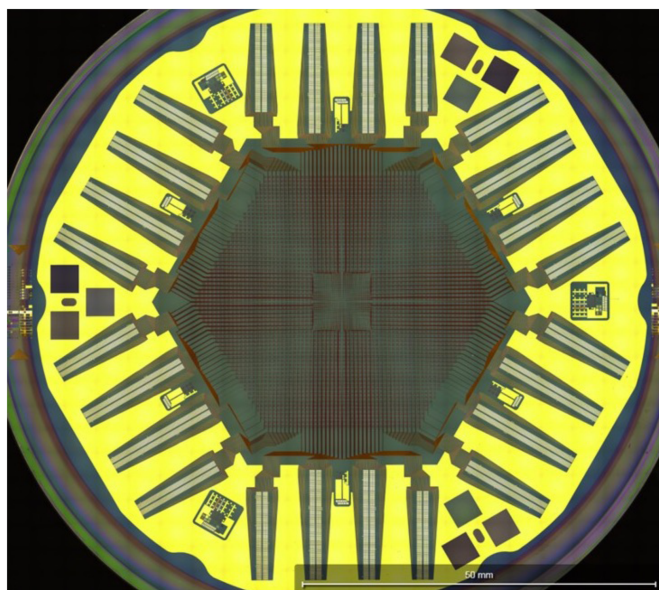
**Fig. 6** LMS FPA magnetic shielding. (a) A photograph of the type of magnetic shields that will be used in the LMS FPA that were developed and tested for the SPICA-Safari instrument concept. (b) This graph shows the excellent agreement between experiment and finite element modeling that has been demonstrated, for the on-axis ratio of the normal component to the internal magnetic field at the detector as a fraction of the applied external field. (c) This plot shows a logarithmic plot of the expected shielding factor within the LMS FPA. (d) The expected shielding factor across the 2-D LEM array.

has a minimum of  $\sim 2200$ , with an average over the detector surface of  $\sim 4000$ , which should be more than sufficient assuming AC fields at a level of  $1 \mu\text{T}_{\text{rms}}$  or less and given the low measured susceptibility of the high-aspect ratio TES thermistors planned for LEM, which require almost 300 times less magnetic shielding than Athena X-IFU detectors prior to reformulation.<sup>19</sup> Figure 6(d) shows how the modeled shielding factor varies over the extent of the LEM focal plane array. Because the shielding factor is limited by effectiveness of the bending into the x-ray entrance aperture, the effective shielding for localized sources (non-uniform fields) can be higher or lower than this, depending upon the location of the source and the resulting position dependence of the field at the FPA. But this is more than sufficient, with a factor of a few margin, at the detector and the SQUID multiplexers, which are the critical locations.

### 3 LEM Detector and Anti-Coincidence Detector

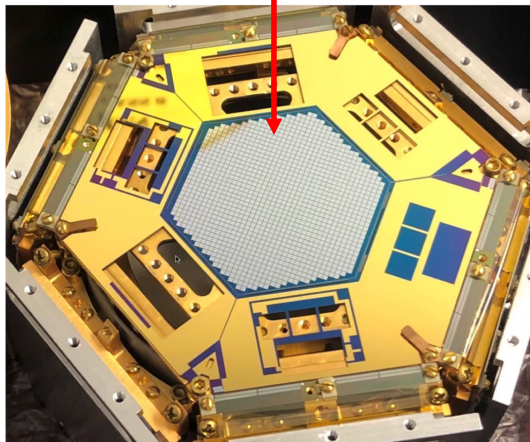
At the core of the LMS is a 14k-pixel microcalorimeter array that provides LEM with unparalleled imaging and spectroscopy capabilities (Fig. 7). The microcalorimeter array provides a  $33^\circ$  FOV using  $15''$  pixels and will operate with a bandpass of 0.2 to 2 keV. The central  $7'$  region of array consists of single pixel TESs with  $\Delta E_{\text{FWHM}} < 1.3$  eV at 1 keV. The remainder of the array comprises 4-pixel hydras with  $\Delta E_{\text{FWHM}} < 2.5$  eV at 1 keV.<sup>38</sup> Hydras consist of four x-ray absorbers, each with a different thermal link to a single TES.<sup>19</sup> The link conductances are tuned to produce a unique pulse shape for x-rays absorbed in each pixel. The pulse rise-time is used to determine which pixel absorbed the photon. The use of hydras allows for the extremely large number of pixels needed for the LEM array, without a proportional increase in the number of wires and circuit components that would otherwise be necessary. In total, the array will have 14k pixels but only 4k TESs. The pixels are arranged on a  $290 \mu\text{m}$  pitch and incorporate  $0.54 \mu\text{m}$  thick Au x-ray absorbers that provide unity stopping power at an energy of 1 keV. The detailed design of the LMS microcalorimeter is described by Smith et al.<sup>19</sup>

The LMS array was assessed at TRL-5 in April 2023 in a NASA/GSFC Technology Readiness Assessment at TRL-5 and benefits from the technical maturity of the Athena/X-IFU microcalorimeter, developed by the same team at GSFC, and shares many common design elements and interfaces.<sup>22</sup> Much of the TRL-5/6 development work completed for the X-IFU,<sup>39,40</sup> including studies on radiation hardness,<sup>41,42</sup> lifetime,<sup>43,44</sup> susceptibility to vibrations, cosmic-ray mitigation, and energy scale calibration has been incorporated into the LMS design.<sup>45</sup> However, the pixel properties have been re-optimized to achieve improved energy resolution within a narrower energy range. In prototype LMS arrays, we have demonstrated both single pixels and hydras with the necessary properties to meet the LEM requirements. Single pixel



**Fig. 7** Layout of a 14k-pixel prototype LMS array.

TESs + Al fins covering Si absorber

**Fig. 8** Photograph of TRL-5 anti-co array.

devices and 4-pixel hydras achieved  $\Delta E_{\text{FWHM}} = 0.9$  and 1.9 eV, respectively, at an energy of 1.5 keV. Position-discrimination in hydra pixels was demonstrated down to 200 eV. These energy resolution and pixel discrimination results and detailed characterizations of the prototype LMS array are described by Wakeham et al.<sup>46</sup> The first full-scale prototype array with the appropriate electrical and mechanical interfaces needed for LEM (Fig. 7) has been fabricated and will be tested in the near future. This array is a precursor to the engineering model (EM) and will demonstrate that the desired performance can be achieved in a full-scale LEM array. Our implementation plan allows for 8 detectors to be fabricated and tested for the engineering model (EM) and 12 for the FM to minimize risk of not meeting all performance requirements.

Given the diffuse and faint nature of LEM's targets, an anti-coincidence detector is crucial to reduce instrument background. Positioned 1 mm directly behind the LEM sensor array, the anti-co flags background events that could be mistaken for a scientific photon within LEM's signal band.<sup>19</sup> The dominant cosmic rays are minimum ionizing particles (MIPs) in the form of protons and alpha particles, which deposit energy continuously as they traverse the main detector array and the anti-co beneath it. Our 12-channel anti-co is based upon large-area detectors that have been developed by the dark matter detection community.<sup>47–49</sup> The anti-co consists of a 0.5 mm thick Si crystal that is covered with a parallel network of TESs + Al athermal phonon cells (Fig. 8) that collect the energy deposited in the Si by the MIPs. In our full-scale prototype, we have demonstrated the 20 keV low-energy detection threshold and the 95% live-time required to meet the LEM science requirements.

#### 4 Cold Readout: Time-Division Multiplexing SQUIDs and Amplifier SQUIDs

Brute-force readout, in which each of the LMS's  $\sim 4000$  TESs had its own amplifier chain, would be enormously challenging due to the wire count, heat load, and general complexity of such a system. Instead, the LMS employs multiplexed readout, or the integration of readout signals from multiple TESs into an amplifier channel. The signal currents from the LMS TESs are read out via the technique of SQUID TDM.<sup>50</sup> Figure 9 illustrates the basics of the TDM readout scheme.

There are  $N_{\text{rows}} = 60$  TDM rows in each LMS readout channel. The row-dwell period is 160 ns; thus, each TES's signal current is sampled once per  $60 * 160 \text{ ns} = 9.6 \mu\text{s}$  readout frame. The pulse time-constants of the (thermal) TESs are much slower—on order of milliseconds—so this scheme is able to sample the TES-signal currents with the fidelity needed. Each readout channel has up to 59 “signal” rows (each of which has a TES input) and at least one “dark” row that either reads out a non-TES resistor or whose FE-SQUID-input circuit is disconnected; the dark pixels are used for diagnostics such as the separation of gain variations in the SQUIDs from those in the TESs.

A nearly identical TDM-readout system to the LMS's is under development by the same NIST/NASA team for the Athena X-IFU.<sup>52–58</sup> A NASA/GSFC technology readiness assessment

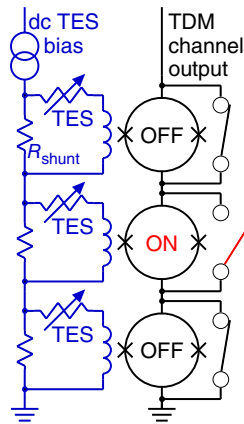


**Fig. 9** Cartoon circuit schematic of TDM operation. Each TES’s signal current is inductively coupled to an FE dc-SQUID (FE-SQUID). A dc-SQUID is a magnetic-flux sensor that has two Josephson junctions in a superconducting loop. One of these SQUIDs at a time per readout channel is activated via sequential operation of superconducting switches. When a switch is opened, its SQUID is activated and its TES’s current is passed up the channel’s readout chain. When switches are closed, their SQUIDs are shorted out and thus do not pass the signal current from their TESs. The TESs are dc-biased and are always on. Rows are switched every 160 ns. The switch-activation (“row-address”) signals are linked across readout channels, such that logical rows of SQUIDs are enabled serially in time while columns are read out in parallel. The FE-SQUID currents are amplified by a second-stage series-array SQUID (amp-SQUID,<sup>51</sup> not shown here) on the LMS FPA’s 350 mK stage and then passed to room-temperature electronics.

(TRA) determined in February 2023 that X-IFU’s TDM readout had reached TRL-5. The studies toward TRL-5 for X-IFU included power dissipation,<sup>52,55,59</sup> component area,<sup>52,58</sup> radiation hardness, the co-microfabrication of TDM-SQUID and TES-bias componentry,<sup>52,58</sup> crosstalk,<sup>54</sup> cold-indium bump bonding of TDM chips to FPA side panels,<sup>53</sup> two-level row-address switching,<sup>52</sup> and performance demonstrations in integrated assemblies.<sup>53,55</sup>

The only differences between X-IFU’s TDM circuitry and the LEM’s are the multiplexing factor (48 for X-IFU versus 60 for the LMS), some electrical-component values (discussed further below), and the form factors of the TDM chips (each X-IFU chip is a  $16 \times 6$  physical array of cells, and each LMS chip is a  $20 \times 9$  array; the TDM pixel sizes are  $1.1 \text{ mm} \times 1.7 \text{ mm}$  in each case). In an assessment based largely on the similarity of the LMS’s readout to X-IFU’s, another NASA/GSFC TRA in April 2023 determined that LEM’s TDM readout (FE-SQUIDs and amp SQUIDs) was also at TRL-5.

The LMS TDM-readout system was designed around the TES detectors (single-pixel and hydra) described in Sec. 3 and further by Smith et al.<sup>19</sup> The single-pixel TESs and the hydra TESs will use the same TES-bias-loop components

- TES-shunt resistor:  $R_{\text{shunt}} = 100 \mu\Omega$ ;
- total inductance in the TES-bias loop:  $L_{\text{loop}} = 1560 \text{ nH}$ ;
- TES-bypass resistor:  $R_{\text{TES-bypass}} = 68 \text{ m}\Omega$ .

With these TES-bias-circuit values, the assumed parameters that are relevant to the design of the LMS readout are

- the maximum TES current-slew rate due to a 2 keV x-ray (the maximum energy of interest to LEM) is budgeted to be  $dI/dt|_{\text{max}} = 0.065 \text{ A/s}$ ;
- the maximum permitted readout white-noise to stay within the energy-resolution budget,<sup>19</sup> referred to as the TES current noise, is  $\sqrt{S_{I\text{-mux}}} = 12 \text{ pA}/\sqrt{\text{Hz}}$ .

Stability in a TDM readout system requires that the maximum flux change within a readout frame, which occurs on the leading edge of a TES pulse at the highest x-ray energy of interest, remains within the roughly linear range of the FE-SQUID’s quasi-sinusoidal input current ( $I$ ) verses magnetic flux ( $\Phi$ ) coupled to the FE-SQUID curve, or

$$\Delta\Phi_{\max} = dI/dt|_{\max} * t_{\text{frame}} * M_{\text{in}} \leq X * \Phi_0,$$

where  $t_{\text{frame}}$  is the frame time,  $M_{\text{in}}$  is the input coupling of TES current to the FE-SQUID, and  $X$  is the fraction of a flux quantum over which the FE-SQUID's response is roughly linear. For  $t_{\text{frame}} = 9.6 \mu\text{s}$ , the maximum slew rate listed above, and  $X \sim 0.30$  (a typical value),<sup>56</sup> the equation above yields  $M_{\text{in}} \leq 995 \text{ pH}$ . We have conservatively chosen  $M_{\text{in}} = 820 \text{ pH}$  for the LMS.

The budgeted value for the power-spectral density (PSD) of the readout white noise (all sources; non-multiplexed; referred to flux in the FE-SQUID) for Athena X-IFU is  $\sqrt{S_{\Phi}} = 0.32 \mu\Phi_0/\sqrt{\text{Hz}}$ . Lab demonstrations of TDM have routinely achieved much better noise performance than this<sup>53,55,56,57</sup> but to be conservative we carry for the LMS this same top-level readout-noise budget. In a TDM system, the multiplexed TES-referred readout-noise PSD<sup>59</sup> is

$$\sqrt{S_{I-\text{mux}}} = M_{\text{in}}^{-1} * \sqrt{(\pi * N_{\text{rows}} * S_{\Phi})}.$$

Thus, if the readout noise were at the budgeted PSD of  $0.32 \mu\Phi_0/\sqrt{\text{Hz}}$ , the TES-referred noise would be  $11.1 \text{ pA}/\sqrt{\text{Hz}}$ , which is within the  $12 \text{ pA}/\sqrt{\text{Hz}}$  requirement of the energy-resolution budget. Thus, the LMS readout design is correctly dimensioned.

The FE dc-SQUIDs (FE-SQUIDs) are located on the side panels of the 40 mK LMS FPA (see Fig. 4), on chips that are cold-indium bump bonded to the side-panel carriers. Each of the six side panels of the LMS 40 mK FPA contains an independent 12-channel X 60-row TDM multiplexer. The bump-bonding process needed for X-IFU and LMS was developed at NIST between 2020 and 2022<sup>53</sup> and flight-like X-IFU TDM devices were successfully tested in late 2022.<sup>52</sup>

Laboratory-style TDM test-chips (containing flight-like close-packed two-dimensional arrays of TDM cells but in a wirebondable configuration for easy use in existing laboratory test systems) with the LMS readout parameters described above were fabricated at NIST in July 2023. These chips are planned to be tested with LEM-like TESs in August and September 2023.

Finally, each TDM channel's SQUID-current signal is amplified by a second-stage series-array SQUID (amp-SQUID) that consists of hundreds of dc-SQUID elements.<sup>51</sup> At the output of the amp-SQUIDs, the readout signals are at appropriate voltage levels to couple to the WFEEs (see Sec. 5).

## 5 LMS Electronics

### 5.1 Warm Front-End Electronics

The WFEE are the analog FEEs that directly interface to the cold circuits, as shown in Fig. 10. The main components of the WFEE are an LNA used to amplify the error signal coming from the AMP squid and a series of digital to analog converter (DAC) to provide biases for various cryogenic components (TES, SQ1, and AMP SQUID). Both the LNA and DACs are provided by an ASIC (application specific IC), where each ASIC chip provides two LNAs and six current DACs. There are three boxes of WFEEs, and each box contains two modules, so six modules in total. There are 6 ASICs in each module and thus 12 LNAs, which then allows for the read-out of the 72 LEM read-out channels. Each module is controlled by the processor in the DEEP via RS-485 and I<sup>2</sup>C interfaces. A prototype ASIC has been developed for the Athena-XIFU, and the performance has been proved to meet the X-IFU and LMS requirements. It is currently undergoing radiation tests. Upon completion of these routine tests, the TRL of the WFEE will advance to TRL-6. A detailed description of the WFEE is provided by Sakai et al.<sup>60</sup>

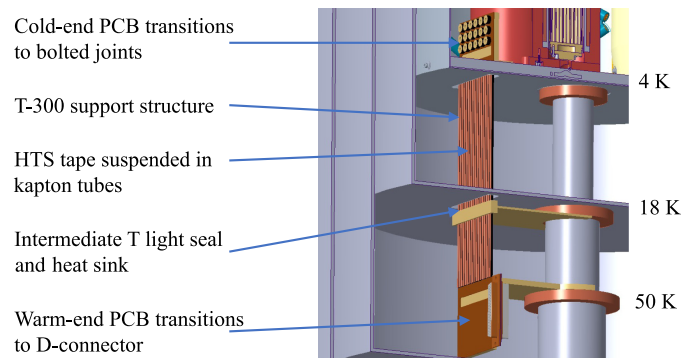
### 5.2 Digital Electronics and Event Processor

The DEEP, also shown in Fig. 10, is the part of the read-out chain in which the signals from each TES are demultiplexed into TES specific streams. Each data stream is then analyzed to detect all x-ray events, discriminate between source pixels (in the case of hydras) and characterize the x-ray events, predominantly by energy and arrival time. There are six DEEP boxes, and each box consists of one row module, three column modules, and one power module. The row module provides the switching signal for SQ1 multiplexers, which it does by generating the row switching timing signals in the FPGA and converting these to differential analog signals using CMOS drivers. The analog voltages are generated using two low-speed DACs. The row module also



**Table 3** Table describing the various LMS harnesses inside the cryostat.

Subsystem	Function	Heritage	Notes
Detection chain	Detector signals	Athena, Micro-X	Based on laboratory and suborbital systems, leveraging Athena designs
ADR	Housekeeping for ADR and FPA	XRISM/Hitomi	Flight heritage Hitomi
ADR	High current leads	XRISM/Hitomi	Flight heritage Hitomi
ApA (filters)	Housekeeping for IR filters	XRISM/Hitomi	Flight heritage Hitomi
Dewar	Housekeeping for dewar	Lockheed-Martin	Flight heritage Gravity Probe-B and WISE

**Fig. 11** This drawing shows how the high temperature superconducting magnet lead harness has been designed to feed through from 50 K to 4 K, with heat-sinking at 18 K, including the terminations.

shield at 100 K. From the pass-through, it loops over to a connector on the 50 K heat sink. These high current leads are cooled down to 50 K are made from phosphor bronze. Below the 50 K stage, high temperature superconductors (HTS) greatly reduce the harness heat load on the cryocooler. The LMS HTS lead assembly will be similar in many respects to those used in the SXS/Hitomi and Resolve/XRISM instruments.<sup>22,24</sup> However, the LMS has a larger number of leads, and the planned lead design is shown in Fig. 11. For the LMS, these are described in more detail in Osborne et al.<sup>21</sup>

The housekeeping harnesses are regular twisted pair wires in looms and support the low bandwidth and low noise readout of thermometry and heaters.

## 6 Aperture Assembly and Filter Wheel

### 6.1 Aperture Assembly and Blocking Filters

The LMS aperture consists of a series of openings in stages at temperatures ranging from 260 K to 40 mK as partially depicted in Fig. 12. The aperture assembly (ApA) defines and constrains these openings, with the primary purpose of blocking radio-frequency, infrared, visible, and ultraviolet radiation via thin-film BFs while allowing x-rays to pass through with minimal absorption. Overall, the ApA is a system of barriers, baffles, filter carriers, and filter mounts that incorporates these filters and inhibits their potential contamination while also complying with budgets for stray light and heat loads at the different dewar stages. The design of the LMS aperture hardware benefits from the experience with the Hitomi/SXS and XRISM/Resolve apertures<sup>61</sup> and photon-noise analysis of preliminary Athena/X-IFU designs.<sup>62</sup>

The LMS has five BFs configured, as shown in Fig. 13 and described in Table 4. To take advantage of the substantial filter development completed for the Athena/X-IFU,<sup>63</sup> the LMS filter designs are based upon the latest X-IFU baseline designs, using identical thin-film composition

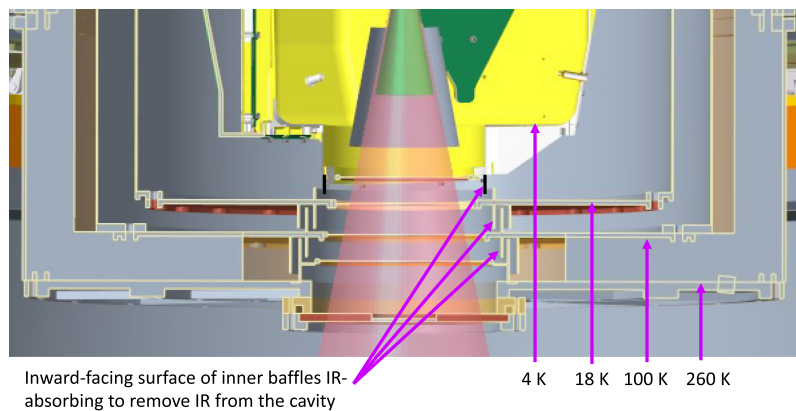


**Fig. 12** Notional layout of the aperture assembly, showing the placement of the filters from 260 to 4 K. Details of the interfaces from each filter to its baffled mount are not shown. Water vapor diffusing out of the multi-layer insulation is gettered by a labyrinth of cold baffles.

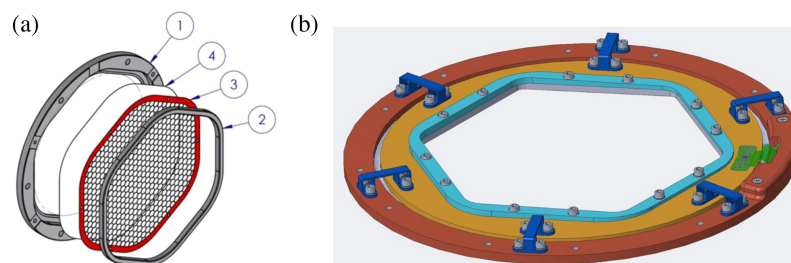


**Fig. 13** (a) Schematic mounting of the film and supporting mesh inside the two-part frame of an Athena/X-IFU filter, on which the LEM filters will be based. 1 is the outer frame, 2 is the inner frame, 3 is the supporting mesh and 4 is the thin polyimide/Al foil (45 nm polyimide/30 nm Al). (b) LEM filter carrier design that allows isolation of the filter temperature from the heat sink due to the low thermal conductance between the two frame parts.

**Table 4** Properties of the series of five optical BFs.

$T$ (K)	Open diameter (mm)	Nominal height above array (mm)	Mesh material	Mesh thick. (mm)	Block. Frac. (%)
260	118	200.0	BeCu with 15 F06Dm Ag + 200 nm Au plating	80	4
100	110	179.0	BeCu + 200 nm Au plating	80	2
18	101	155.0	BeCu + 200 nm Au plating	80	2
4	94	134.5	BeCu + 200 nm Au plating	80	2
0.04	51	16.7	Nb	80	4

(45 nm polyimide and 30 nm Al) supported by metallic meshes (BeCu for all filters except the 40 mK, which uses Nb) with hexagon cell widths of  $\sim 5$  mm. The clear aperture requirements for the LMS filters are similar to those for X-IFU.<sup>24,64</sup>

The three warmer filters (mounted to stages at 260, 100, and 18 K) will be installed in carrier rings with decontamination heaters and control thermometers, similar to SXS and Resolve. This design, as shown in Fig. 13, ensures that the three outer filters can be heated above the temperatures of the shields they are connected to with relatively low power (W scale). The good thermal conductivity across the metal meshes ensures good thermalization across the filters. The outer filter, which faces the interior of the spacecraft, will be controlled so that no portion of the filter is

<300 K to inhibit sticking of organic volatiles. The heaters on the 100 and 18 K stages are intended for use during cooling down of the dewar to ensure that the surrounding baffles cool before the filters but could also be used for decontamination.

Because larger filters are needed for LEM than were flown on Hitomi/SXS or have been yet fully qualified for Athena/X-IFU, the ApA is considered to be at TRL-5. But the mesh-supported filters are able to scale to a larger filter size without necessarily becoming more fragile and thus there is a relatively straightforward engineering path needed to establish TRL-6. Prior to going into the implementation phase, the LEM ApA team will validate the LMS mechanical and thermal designs of filter-carrier assemblies integrated into the associated mounts via vibration tests, thermal-cycle tests, and thermal characterization.

## 6.2 Filter Wheel Assembly

The filter wheel assembly consists of the filter wheel mechanism (FWM) with various filters attached and the mechanism control electronics (MCEs) that control the FWM. The FWM is attached to the LEM telescope optical bench and is situated in front of the FPA, and the mechanical design is depicted in Fig. 14. This mechanism is needed to allow different filters to be inserted into the x-ray beam depending on the astrophysical observation that is being made, to ensure that the detector performance and throughput does not suffer from too high a flux of x-rays. The FWM has seven positions, including one open, one closed, and one for radioactive source and four filters with different transmissions, moved via a single actuator. Optical BFs on this filter wheel are desirable to limit the optical load from the bright UV photons that are emitted from some x-ray sources. A neutral density filter will also allow for a reduction of count-rate while looking at, for example, some supernova remnants.

Filter wheels have flown on other space telescopes and including x-ray missions such as Hitomi<sup>22</sup> and IXPE.<sup>65</sup> For the LEM FWA, the design incorporates elements from current and past missions such that all engineering that is necessary maintains a TRL of TRL-6. The filter designs on the FWA are based upon Athena filters but with a slightly larger diameter.

The FWM is controlled by the MCE, and Table 5 describes the overall environment, mass, and power.

The MCE is a two-board design. This basic electronics box provides typical electrical control functionality of the FWM, and the electronics have been chosen that are space qualified and reliability. The technical readiness is TRL-6.

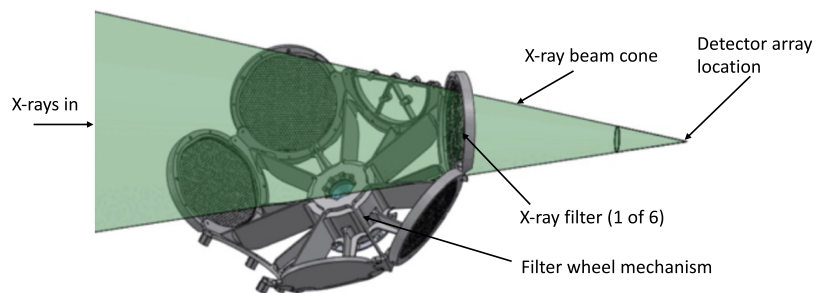


**Fig. 14** The FWM filter in the path of the x-ray beam.

**Table 5** LEM filter wheel assembly environment, mass, and power.

FWA	TRL	Envelope	Mass - CBE (kg)	Nominal power (W)	Peak power (W)
FWM	6	44.4 cm × 71.1 cm (H × D)	7.9	5.5	17.0
MCE	6	7.6 cm × 20.4 cm × 20.4 cm (H × L × W)	3.4	6.7	12.5

## 7 Cryogenic Cooling System Summary

The LMS cryogenic cooling system is depicted in Fig. 2. The architecture evolved from a cooling system concept that was developed for the Lynx x-ray microcalorimeter.<sup>66</sup> There is also a lot of heritage from previous microcalorimeter missions, such as Astro-E, Suzaku,<sup>24</sup> and Hitomi.<sup>22</sup> The cryogenic cooling system consists of a cryocooler, a dewar, and a CADR.

The dewar design was developed by Lockheed Martin<sup>21</sup> and makes use of a reentrant thrust tube design made out of composite tube support structures that have flight heritage from Gravity Probe-B<sup>67</sup> and the Wide-field Infrared Survey Explorer (WISE).<sup>68</sup> The dewar outer shell is passively cooled to 260 K. Two thermal shields at 100 and 18 K are actively cooled by a cryocooler as well as the 50 and 4.0 K cooling stages. This cooling is provided by a four-stage pulse tube cryocooler.<sup>21</sup>

Cooling is needed at 4.0 K primarily to remove the heat generated by the CADR and the FPA and also to remove conducted heat loads from the signal-chain harness and structural support of the whole 4.0 K core as well as some other minor headload sources. The LMS cryocooler designed by Lockheed Martin is based on another cryocooler that was developed as part of advanced cryocooler technology development program (ACTDP).<sup>69</sup> The ACTDP cryocooler has since been tested and qualified for a Balloon flight<sup>70</sup> by ASTHROS,<sup>71</sup> which will be launched in 2023. Table 6 provides a summary of the expected cryocooler heat loads from thermal modeling of the LMS design, and the power needed to operate this cryocooler is 626 W. Because the CADR heat load already incorporates 100% cooling power margin at 40 mK and 50% at 350 mK, there is no need to double-count the margin with additional margin specifically at the cryocooler level from the CADR. The cryocooler control electronics (CCEs) is fully redundant to provide a reliability of >95% for the CCE over 5 years. Together with a TMU reliability of >98.3%, the overall cryocooler reliability is >93% over the LEM mission lifetime. The CCE design is based on the modular advanced cryocooler electronics (MACEs) system developed by Iris Technology Corporation.<sup>72</sup> The Iris MACE can provide accurate command and control for cryocoolers requiring up to 1000 W. Both cryocooler and CCE are TRL-5, and a funded plan exists to advance to TRL-6 before the LEM Mission preliminary design review (PDR).

Continuous cooling is provided at 40 mK for the microcalorimeter detectors and also at 350 mK by a CADR with seven salt pills. These salt pills are split between two stages, one for cooling from 4.0 K to 350 mK and the other to cool from 350 to 40 mK. The detailed design is described by Jahromi et al.<sup>73</sup> The components salt pills and heat switches are all high-TRL optimized in an arrangement to best provide the needed LEM cooling powers while dissipating heat relatively uniformly. The component salt pills and most heat switches have flight heritage

**Table 6** Summary of the heat loads at each cooling stage of the pulse-tube cryocooler. The total heat loads for each temperature stage are shown in bold.

	Stage 4	Stage 3	Stage 2	Stage 1
Unit (W)	4 K load	18 K load	50 K load	100 K load
Harness loads at each stage	0.005	0.023	0.689	2.6
CADR heat load	0.014	—	—	—
Filters	0.001	0.018	—	0.51
Support cylinder	0.006	0.229	0.009	2.73
18 K shield	—	—	0.005	−0.044
50 K plate	—	—	—	−0.084
100 K shield	—	0.044	0.126	—
Vacuum shell	—	—	—	1.15
<b>Total loads for cryocooler</b>	<b>0.026</b>	<b>0.31</b>	<b>0.83</b>	<b>6.90</b>

from Astro-H/Hitomi and XRISM. The CADR is controlled by electronics (adiabatic demagnetization refrigerator controller), which has flight heritage from Astro-H and XRISM.

## 8 LMS Thermal System Design

The LMS thermal control system (excluding the LMS cryogenic cooling system) removes the power that is predominantly from the read-out electronics and cryocooler compressor at an operating temperature of  $\sim 260$  K. The total power from the electronics boxes is given in Table 6. The highest power electronics, the DEEP and CCE boxes, are mounted directly to five radiators that surround the cryostat. The three WFEE boxes are mounted above the top of the dewar to keep the signal chain harness as short as possible and they are connected to a radiator by thermal straps. The cryocooler compressor is also directly connected to a radiator. The warm flange on the top of the dewar is connected to a radiator by two heat pipes. There are MLI covers on both the Sun-facing and the spacecraft-facing sides of the shades that block a direct path to the LMS dewar at all times.

## 9 System Design

The block diagram for the LMS is encompassed in the overall LEM observatory block diagram, as shown in Fig. 15. The diagram shows how the whole observatory has been designed to accommodate the payload, which primarily consists of the x-ray mirror assembly (XMA) and the LMS. It shows the two redundant CCEs that are needed to power the cryocooler and the segmented WFEEs and DEEPs. The DEEPs are responsible for sending out the data signals and receiving commands from the spacecraft. Power for all the electronics boxes is received directly from the spacecraft.

We have developed a detailed master equipment list for the LMS and have made detailed estimates for the required mass, power, and data rate that are detailed in Tables 7 and 8 below. Our current best estimate for the mass is 368 kg. This is dominated by the mass of the dewar and cryocooler (122 kg) and the mass of the electronics boxes (113 kg). The total average power needed during normal operation is  $\sim 1.3$  kW. The total power is largely driven by the power needed for the cryocooler and the DEEP electronics box.

The overall mass is estimated to be 372 kg, including the thermal and structural components of the LMS connected to the optical bench in addition to the main cryostat and electronics. This mass is more than six-times less than the Athena Science Instrument Module prior to reformulation.<sup>22</sup> The lower mass is largely achieved through having the simple single-instrument architecture with a microcalorimeter cooling system design that has just one high reliability cryocooler, rather than the large number of cryocoolers previously baselined for the Athena X-IFU. Overall, the low mass, very modest power dissipation, low data rate and shorter focal

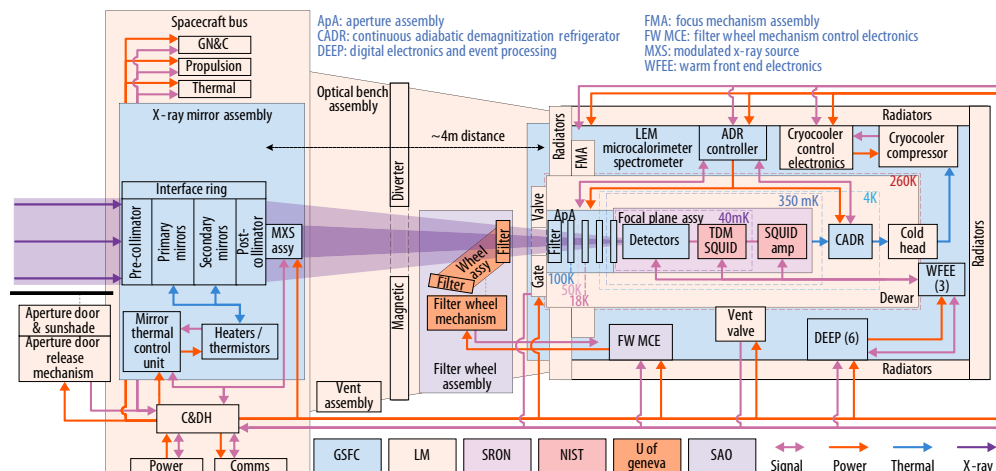


Fig. 15 Block diagram of the LEM telescope.

**Table 7** The mass and power of the main components of the LMS. The sums of the mass and power contributions are provided in bold at the bottom of the table.

	Mass		Power	
	CBE (kg)	CBE power (W)		
		Nominal	Peak	
Aperture assembly	4.5	—	—	
Focusing mechanism	19.6	—	—	
4 K core assembly	37.8	—	—	
WFEE	18.0	32.7	42.5	
DEEP	65.4	543.0	705.9	
CADR controller	29.3	60.8	63.8	
Dewar	88.0	—	—	
Cryocooler	41.0	650.0	780.0	
Instrument thermal	21.3	—	—	
LMS structure	38.2	—	—	
LMS harness	18.9	—	—	
<b>LMS total</b>	<b>382.1</b>	<b>1286.5</b>	<b>1592.3</b>	

**Table 8** Breakdown of the data rate for the LMS and LEM.

	Date rate
LMS typical science data rate	37.1 kbit/s
LMS maximum science data rate	5.3 Mbit/s
LMS and XMA housekeeping data rate	12.0 kbit/s
LEM typical total data rate	77.1 kbit/s
LEM maximum total data rate	5.4 Mbit/s

length translates into lower relative complexity for accommodating the LEM microcalorimeter instrument than for Athena, allowing LEM to fit comfortably within the Probe cost limit.

## 10 Technical Readiness Level Advancement Plan

Each of the critical component technologies that are part of the LMS is listed in Table 9. All these technologies are at least at TRL-5<sup>74,75</sup> and have completed demonstrated component and/or brassboard validation in relevant environment as described in the prior sections. These TRL-levels in Table 9 were confirmed at an independent NASA/GSFC Technology Readiness Assessment in April of 2023 except for the anti-coincidence detector, which was TRL-4 at that time. For TRL-6,<sup>74,75</sup> a system/subsystem model or prototype demonstration in a relevant environment is needed. There remain some milestones to complete the various TRL-6 component and sub-system level development. These are focused on adapting high heritage components already developed specifically to meet the LEM requirements. This work is on-going and expected to be completed well before the instrument PDR.

**Table 9** Component technology readiness level of all critical technologies in the LMS.

Sub-system	LMS element description	Current TRL	Note
FPA	Microcalorimeter array	5	TRL 6 in CY 25
FPA	TDM SQUID multiplexer	5	TRL 6 in CY 25
FPA	Anti-coincidence detector	5	TRL 6 in CY 25
FPA	Mechanical FPA	5	TRL 6 in CY 25
Detection chain	WFEE	5	TRL 6 in CY 24
Detection chain	DEEP	6	
APA	APA	5	TRL 6 in CY 25
Cryogenics	Cryostat	6	
Cryogenics	Cryocooler thermo-mechanical unit	5	TRL 6 in CY 26
Cryogenics	Cryocooler electronics	5	TRL 6 in CY 26
Cryogenics	CADR	5	TRL 6 in CY 25

### 10.1 Microcalorimeter Array and Anti-Coincidence Detector

The LEM sensor array and anti-co detector are on track to achieve TRL-6 by mid-2025. Final component-level TRL-6 verification tests will be completed by the end of 2024. Cosmic-ray background tests previously conducted on the Athena/X-IFU microcalorimeter will be repeated on the high-fidelity LMS to validate the array's thermal design. Vibration testing and thermal cycling of high-fidelity detector and anti-coincidence detector prototypes, mounted to flight-like sub-assemblies, are planned for phase-A in mid-2024. The arrays will undergo pre- and post-vibe testing to confirm that the yield and detector performance remain unchanged. The array will be connected to two high-fidelity side panels with bump-bonded TDM multiplexor chips, enabling the readout of 12 TDM channels. Flight-like second stage amplifier SQUID chips will be integrated at the 350 mK stage of the platform.

### 10.2 Cold Readout

The cold readout (TDM FE-SQUIDs and amp-SQUIDs) will reach TRL-6 by mid-2025. During 2024 and early 2025, a high-fidelity 40 mK FPA will be built and tested as described below for the TRL-6 system level tests. We will fully populate and test two readout side panels; each side panel will be in its flight configuration with four bumped 3-column X 60-row TDM chips. The 350 mK stage of our TRL-6 platform will include high-fidelity amp-SQUIDs for the 24 active TDM-readout channels. The suite of readout-specific tests will include verification of the required readout noise and common-mode rejection of the LMS differential-readout scheme.

### 10.3 Mechanical FPA

To advance to TRL-6, the LEM design scaled from X-IFU needs to be consolidated and some of the key interfaces need to be adapted. In particular, the design of the interface between the LEM anticoincidence detector and FPA needs further refinement. The exact routing of harnesses within the FPA and the external signal chain harness also needs refinement. A demonstration of the 50 mK assembly with the full-size LEM detector chips is needed to verify the eigenfrequencies during vibration and for mechanical testing under thermal cycling. The Kevlar suspension with the higher precise LEM masses and suspension will be demonstrated and again tested for the eigenfrequencies and demonstration of ability to withstand the launch loads.

### 10.4 Continuous Adiabatic Demagnetization Refrigerator

The technology development plan for the CADR is focused on adapting the high heritage components already developed for XRISM to meet the specific LEM requirements. It includes

vibration testing and qualification of the internal mechanical support for some stages. This is accomplished via vibration testing of dummy masses suspended identically to the baselined stages to achieve TRL-5. Development of a five-stage CADR began in November 2022, consisting of two LEM-like upper parallel stages for continuous platform cooling at 1 K and three serially configured lower stages. There will be further development of stages between 1.2 K and 350 mK specifically for the LEM design including the optimization of heat switches.

### 10.5 Blocking Filters and Aperture Assembly

To raise the TRL to 6, the mechanical and thermal designs of EM filter-carrier assemblies will be validated and integrated into the associated mounts via vibration tests, thermal-cycle tests, and thermal characterization. Phase A effort will deal with the extremes—the main-shell filter and the 40-mK filter. The main-shell filter is a priority because of its size and need of continuous heating for decontamination. The 40-mK filter is the next highest priority because of the different material of its mesh (Nb instead of BeCu) and because the equivalent filter for X-IFU is about half the diameter of what is needed for LEM. The remaining filter assemblies will be verified in phase B, prior to PDR.

### 10.6 Cryocooler

Both the cryocooler and control electronics are currently at TRL-5, with a plan in place to raise the TRL-6 by the 2026. For the cryocooler, there is a need to build a new compressor that is “build-to-print.”<sup>3</sup> He will be used to achieve the required cooling power at 4.0 K, in a demonstration that will verify the cooling power at each of the four-stages of the cryocooler. The dewar is TRL-6, but some additional engineering work will be carried out to demonstrate the needed cylinder support shrink fit cooling between stages for the specific LEM design. The cylindrical shrink fit connections use the differential thermal contraction of different materials to provide excellent thermal contact upon cooling. These tubes are machined to a tight tolerance, in a compact geometry, as has been demonstrated in prior space cryostat designs.<sup>67,68</sup>

### 10.7 System-Level TRL-6 Tests

An important part of TRL-6 is to complete system-level tests. While more than a dozen complete working systems consisting of TES microcalorimeters and TDM multiplexed read-out have been fielded by the NIST and GSFC cryogenic detector groups, including the sub-orbital Micro-X payload, it is necessary to have a full read-out chain test with high-fidelity components that meets the LEM requirements of the critical components and that only need to be scaled in number for a full system-level TRL-6 demonstration. This system must also demonstrate that it meets the critical interface requirements of the other LMS sub-systems. An integrated system-level demonstration will be carried out at GSFC in 2025 to verify the full detection chain using the differential readout architecture baselined for the LMS. This demonstration will involve a high-fidelity LMS array and high-fidelity side-panels with LEM-like 2-D TDM multiplexing chips designed to meet the form, fit, and function requirements of LEM. The system will utilize differential harnessing, prototype LMS room temperature electronics, and amp SQUIDs operating at 350 mK (as planned LEM), to provide a validation of the full detection chain prototype prior to the Engineering Model development in the mission Phase-B. In parallel, a similar system-level demonstration model for the Athena X-IFU will be developed, utilizing an Athena (LEM-like) mechanical FPA with a TES microcalorimeter read out using TDM multiplexing and a differential architecture as well. The components used will be similar to the GSFC demonstration.

Currently, LEM is a proposed mission concept. After demonstration of TRL-6 for all the critical technologies, if the proposal is accepted, the plan for the LMS implementation is to develop a full EM of the 4-K core and the entire read-out detection chain, as well as the aperture assembly prior to building the flight model. There will also be flight spares of all the critical components of all LMS subsystems.

## 11 Conclusions

We have developed a detailed design concept for the LMS that meets the LEM technical requirements, and is designed using mature technologies. We have described a solid plan

to complete the maturation to TRL-6 for all critical technologies. The key driving technologies, such as the microcalorimeter array, the TDM multiplexed read-out, and the mechanical FPA, have a high maturity level due to the decades of support from the x-ray astrophysics community and also the leveraging of a large amount of support by NASA and ESA in the technology developments for the Athena X-IFU. The cooling system also leverages components from years of developments of ADRs for prior astrophysics missions, and an advanced development of the CADR concept also supported by NASA. It utilizes a single highly reliable 4-K cryocooler technology that is able to accommodate the heat loads of the LMS with all the appropriate margins for a space mission and is able to do so using an existing and proven compressor design for which no new development is needed. The mass of the LMS and the power needed to operate the instrument are relatively modest and well within the capabilities of the LEM spacecraft. The capabilities of the LMS with its shorter focal length and optimization for lower energies, opens up a whole new realm of astrophysical observations and will allow us to fill in a major missing puzzle piece in our understanding of cosmic ecosystems.

---

### Data Availability

Data sharing is not applicable to this article, as no new data were created or analyzed.

### Acknowledgments

The material is based upon work supported by NASA internal scientist funding model (ISFM) “Advanced X-ray Microcalorimeters.” The material is also based upon work supported by CRESST under NASA (Grant No. 80GSFC21M000).

### References

1. R. Kraft et al., “Line Emission Mapper (LEM): probing the physics of cosmic ecosystems,” (2022).
2. National Academies of Sciences and Medicine, “Pathways to discovery in astronomy and astrophysics for the 2020s,” The National Academies Press, Washington, DC (2021).
3. J. N. Bregman et al., “The extended distribution of baryons around galaxies,” *ApJ* **862**, 3 (2018).
4. J. N. Bregman et al., “Hot Extended Galaxy Halos around Local L\* Galaxies from Sunyaev–Zeldovich measurements,” *ApJ* **928**, 14 (2022).
5. Y. Faerman et al., “Massive warm/hot galaxy coronae as probed by UV/X-ray oxygen absorption and emission. I. Basic model,” *ApJ* **835**, 52 (2017).
6. S. D. M. White and C. S. Frenk, “Galaxy formation through hierarchical clustering,” *ApJ* **379**, 52 (1991).
7. M. S. Peebles et al., “A budget and accounting of metals at  $z \sim 0$ : results from the COS-Halos survey,” *ApJ* **786**, 54 (2014).
8. J. Tumlinson et al., “The circumgalactic medium,” *Annu. Rev. Astron. Astrophys.* **55**, 389–432 (2017).
9. C. F. McKee and E. C. Ostriker, “A theory of the interstellar medium: three components regulated by supernova explosions in an inhomogeneous substrate,” *ApJ* **218**, 148 (1977).
10. D. P. Cox, “The three-phase interstellar medium revisited,” *Annu. Rev. Astron. Astrophys.* **43**, 337–385 (2005).
11. C.-G. Kim and E. C. Ostriker, “Three-phase interstellar medium in galaxies resolving evolution with star formation and supernova feedback (TIGRESS): algorithms, fiducial model, and convergence,” *ApJ* **846**, 133 (2017).
12. R. Weaver et al., “Interstellar bubbles. II. Structure and evolution,” *ApJ* **218**, 377 (1977).
13. P. F. Hopkins et al., “Galaxies on FIRE (feedback in realistic environments): stellar feedback explains cosmologically inefficient star formation,” *Mon. Not. R. Astron. Soc.* **445**(1), 581–603 (2014).
14. C.-G. Kim and E. C. Ostriker, “Numerical simulations of multiphase winds and fountains from star-forming galactic disks. I. Solar neighborhood TIGRESS model,” *ApJ* **853**, 173 (2018).
15. M. E. Orr et al., “Bursting bubbles: feedback from clustered supernovae and the trade-off between turbulence and outflows,” *ApJ* **932**, 88 (2022).
16. R. A. Chevalier and A. W. Clegg, “Wind from a starburst galaxy nucleus,” *Nature* **317**, 44–45 (1985).
17. R. McCray and M. Kafatos, “Supershells and propagating star formation,” *ApJ* **317**, 190 (1987).
18. J. R. Dawson, “The supershell - molecular cloud connection: large-scale stellar feedback and the formation of the molecular ISM,” *Publ. Astron. Soc. Australia* **30**, e025 (2013).

19. S. J. Smith et al., “Design of the microcalorimeter and anti-coincidence detector for the Line Emission Mapper,” *J. Astron. Telesc. Instrum. Syst.* **9**(4), 041005 (2023).
20. I. Ferreira et al., “Design of the charged particle diverter for the ATHENA mission,” *Proc. SPIE* **10699**, 106994A (2018).
21. E. Osborne et al., “Line emission mapper cryogenic system design,” *J. Astron. Telesc. Instrum. Syst.* **9**(4) (2023).
22. Y. Ishisaki et al., “Status of resolve instrument onboard x-ray imaging and spectroscopy mission (XRISM),” *Proc. SPIE* **12181**, 121811S (2022).
23. R. Kelley and K. Nakazawa, “Special Section Guest Editorial: the Hitomi X-Ray Observatory, Part 2, and 11 references within special section,” *J. Astron. Telesc. Instrum. Syst.* **4**(2), 021401 (2018).
24. K. Mitsuda, “The x-ray observatory Suzaku,” *Publ. Astron. Soc. Japan* **59**(sp1), S1–S7 (2007).
25. A. Hubbard et al., “First flight performance of the “micro-x microcalorimeter x-ray sounding rocket,”” *J. Astron. Telesc. Instrum. Syst.* **9**(3), 034001 (2023).
26. A. S. Hoover et al., “Uncertainty of plutonium isotopic measurements with microcalorimeter and high-purity germanium detectors,” *IEEE Trans. Nucl. Sci.* **61**, 2365–2372 (2014).
27. D. A. Bennett et al., “A high resolution gamma-ray spectrometer based on superconducting microcalorimeters,” *Rev. Sci. Instrum.* **83**, 093113 (2012).
28. D. A. Wollman et al., “High-resolution, energy-dispersive microcalorimeter spectrometer for x-ray microanalysis,” *J. Microsc.* **188**, 196–223 (1997).
29. J. Uhlig et al., “High-resolution x-ray emission spectroscopy with transition-edge sensors present performance and future potential,” *J. Synchrotron. Radiat.* **22**, 766–775 (2015).
30. G. L. Betancourt-Martinez et al., “The transition-edge EBIT microcalorimeter spectrometer,” *Proc. SPIE* **9144**, 91443U (2014).
31. M. R. J. Palosaari et al., “Transition-edge sensors for particle induced x-ray emission measurements,” *J. Low Temp. Phys.* **176**, 285–290 (2013).
32. J. Uhlig et al., “Table-top ultrafast x-ray microcalorimeter spectrometry for molecular structure,” *Phys. Rev. Lett.* **110**, 138302 (2013).
33. S. Okada et al., “High-resolution kaonic-atom x-ray spectroscopy with transition-edge-sensor microcalorimeters,” *J. Low Temp. Phys.* **176**, 1015–1021 (2014).
34. Z. H. Levine, “X-ray computed tomography,” November 8, 2016, <https://www.nist.gov/programs-projects/x-ray-computed-tomography-ct> (accessed 10 March 2021).
35. B. Jackson et al., “The focal plane assembly for the Athena x-ray integral field unit instrument,” *Proc. SPIE* **9905**, 990521 (2016).
36. W. Jellema et al., “The SAFARI far-infrared instrument for the SPICA space telescope,” in *OSA Technical Digest*, Optica Publishing Group, p. FW3B.3 (2018).
37. A. Bergen et al., “Design and validation of a large-format transition edge sensor array magnetic shielding system for space application,” *Rev. Sci. Instrum.* **87**(10), 105109 (2016).
38. S. J. Smith et al., “Multiabsorber transition-edge sensors for x-ray astronomy,” *J. Astron. Telesc. Instrum. Syst.* **5**, 021008 (2019).
39. S. V. Hull et al., “Characterizing thermal background events for Athena X-IFU,” *IEEE Trans. Appl. Supercond.* **33**(5), 1–6 (2023).
40. S. J. Smith et al., “Correcting gain drift in TES detectors for future x-ray satellite missions,” *IEEE Trans. Appl. Supercond.* **33**(5), 1–6 (2023).
41. K. Sakai et al., “Demonstration of a full-scale brassboard TES microcalorimeter array for the Athena X-IFU,” *IEEE Trans. Appl. Supercond.* **33**(5), 1–6 (2023).
42. S. Beaumont, “Long term performance stability of transition-edge sensor detectors,” *IEEE Trans. Appl. Supercond.* **33**(5), 1–6 (2023).
43. S. Beaumont et al., “Effect of space radiation on transition-edge sensor detectors performance,” *IEEE Trans. Appl. Supercond.* **33**(5), 1–6 (2023).
44. S. J. Smith et al., “Performance of a broad-band, high-resolution, transition-edge sensor spectrometer for x-ray astrophysics,” *IEEE Trans. Appl. Supercond.* **31**(5), 2100806 (2021).
45. A. R. Miniussi et al., “Thermal crosstalk measurements and simulations for an x-ray microcalorimeter array,” *J. Low Temp. Phys.* **199**(3–4), 663–671 (2020).
46. N. A. Wakeham et al., “Characterization of the microcalorimeters developed for the Line Emission Mapper,” *J. Astron. Telesc. Instrum. Syst.* **9**(4) (2023).
47. C. N. Bailey et al., “Development of a TES-based anti-coincidence detector for future x-ray observatories,” *J. Low Temp. Phys.* **167**(3–4), 236–241 (2012).
48. S. E. Busch et al., “Characterization of a prototype TES-based anti-coincidence detector for use with future x-ray calorimeter arrays,” *J. Low Temp. Phys.* **184**(1–2), 23–29 (2016).
49. R. Ren et al., “Design and characterization of a phonon-mediated cryogenic particle detector with an eV-scale threshold and 100 keV-scale dynamic range,” *Phys. Rev. D* **104**(3), 032010 (2021).

50. H. Akamatsu et al., “Signal readout for transition-edge sensor x-ray imaging spectrometers,” in *Handbook of X-ray and Gamma-ray Astrophysics*, C. Bambi and A. Santangelo, Eds., Springer (2023).
51. R. P. Welty and J. M. Martinis, “A series array of DC SQUIDs,” *IEEE Trans. Magn.* **27**(2), 2924–2926 (1991).
52. M. Durkin et al., “Symmetric time-division-multiplexed SQUID readout with two-layer switches for future TES observatories,” *IEEE Trans. Appl. Supercond.* **33**, 1–5 (2023).
53. T. J. Lucas et al., “Indium bump process for low-temperature detectors and readout,” *J. Low Temp. Phys.* **209**, 293–298 (2022).
54. M. Durkin et al., “Mitigation of finite bandwidth effects in time-division-multiplexed SQUID readout of TES arrays,” *IEEE Trans. Appl. Supercond.* **31**, 1–5 (2021).
55. S. J. Smith et al., “Performance of a broad-band, high-resolution, transition-edge sensor spectrometer for x-ray astrophysics,” *IEEE Trans. Appl. Supercond.* **31**, 1–6 (2021).
56. M. Durkin et al., “A predictive control algorithm for time-division-multiplexed readout of TES microcalorimeters,” *J. Low Temp. Phys.* **29**, 2101005 (2020).
57. M. Durkin et al., “Demonstration of Athena X-IFU compatible 40-row time-division-multiplexed readout,” *IEEE Trans. Appl. Supercond.* **29**, 1–5 (2019).
58. W. B. Doriese et al., “Optimization of time- and code-division-multiplexed readout for athena X-IFU,” *IEEE Trans. Appl. Supercond.* **29**, 1–5 (2019).
59. W. B. Doriese et al., “Progress toward kilopixel arrays: 3.8 eV microcalorimeter resolution in 8-channel SQUID multiplexer,” *Nucl. Instrum. Method Phys. Res. A* **559**, 808–810 (2006).
60. K. Sakai et al., “Development of space-flight room-temperature electronics for the LEM microcalorimeter spectrometer,” *J. Astron. Telesc. Instrum. Syst.* **9**(4), 041004 (2023).
61. C. A. Kilbourne et al., “Design, implementation, and performance of the Astro-H soft x-ray spectrometer aperture assembly and blocking filters,” *J. Astron. Telesc. Instrum. Syst.* **4**(1), 011215 (2018).
62. U. Lo Cicero et al., “X-ray microcalorimeter photon shot noise calculation by ray-tracing simulations: the Athena X-ray integral field unit case study,” (2023).
63. M. Barbera et al., “The thermal filters of the Athena x-ray integral field unit: preliminary design and technology readiness assessment,” (2023).
64. M. Barbera et al., “Filters for x-ray detectors on space missions,” in *Handbook of X-ray and Gamma-ray Astrophysics*, C. Bambi and A. Santangelo, Eds., Springer, Singapore (2022).
65. P. Soffitta et al., “The instrument of the imaging x-ray polarimetry explorer,” *Astron. J.* **162**, 208 (2021).
66. M. DiPirro et al., “Lynx x-ray microcalorimeter cryogenic system,” *J. Astron. Telesc. Instrum. Syst.* **5**(2), 021006 (2019).
67. C. W. F. Everitt et al., “Gravity Probe B cryogenic payload,” *Class. Quantum Gravity* **32**(22), 224009 (2015).
68. E. L. Wright et al., “The Wide-field Infrared Survey Explorer (WISE): mission description, and initial on-orbit performance,” *Astron. J.* **140**, 1868 (2010).
69. R. G. Ross, Jr. and R. F. Boyle, “An overview of NASA space cryocooler programs – 2006,” in *Proc. Int. Cryocooler Conf.*, Annapolis, MD, 14-16 June 2006, Cryocoolers, Vol. 14 (2006).
70. J. R. Olson et al., “Development of a space-type 4-stage pulse tube cryo-cooler for very low temperature,” *Adv. Cryog. Eng.* **51**, 623–631 (2005).
71. J. V. Siles et al., “ASTHROS - astrophysics stratospheric telescope for high-spectral resolution observations at submillimeter-waves: mission overview and development status,” in *Proc. 31st Symp. Space Terahertz Technol., ISSTT 2020*, p. 17 (2020).
72. IRIS Technology, <https://www.iris-technology.com/aerospace/control-electronics>.
73. A. Jahromi et al., “The compact and efficient continuous adiabatic demagnetization refrigerator for LEM,” *J. Astron. Telesc. Instrum. Syst.* **9**(4), 041003 (2023).
74. NASA Procedural Requirements, “NASA space flight program and project management requirements - NPR 7120.5F,” [https://www.humphreys-assoc.com/evms/evms-documents/nasa/NASA\\_N\\_PR\\_7120\\_005FAugust2021\\_.pdf](https://www.humphreys-assoc.com/evms/evms-documents/nasa/NASA_N_PR_7120_005FAugust2021_.pdf).
75. Office of the Chief Engineer, National Aeronautics and Space Administration (NASA), “NASA systems engineering handbook,” NASA/SP-2007-6105 Rev1. [https://soma.larc.nasa.gov/mmx/pdf\\_files/NASA-SP-2007-6105-Rev-1-Final-31Dec2007](https://soma.larc.nasa.gov/mmx/pdf_files/NASA-SP-2007-6105-Rev-1-Final-31Dec2007)

**Simon R. Bandler** is a research astrophysicist at NASA’s Goddard Space Flight Center. He received his BS degree in mathematical physics from the University of Sussex in the United Kingdom and his MS and PhD degrees in physics from Brown University in 1992 and 1996, respectively. He is the author of more than 200 journal papers. His current research

interests include transition-edge sensor and magnetic x-ray microcalorimeters, x-ray astrophysics, and the ESA flagship mission called Athena.

**Edward G. Amatucci** is an instrument systems engineer as a contractor for NASA Goddard Space Flight Center. He earned a bachelor of science degree in mechanical engineering from the University of Maryland and a master of engineering degree in mechanical engineering as well as a master of science degree in technical management from Johns Hopkins University. He has 17 years of experience in precision engineering and robotics from the National Institute of Standards and Technology as well as 22 years of experience at NASA working on various missions including MESSENGER, JWST, and other projects as an instrument manager and as an instrument systems engineer.

**Michael J. DiPirro** received his PhD in low-temperature physics from the State University of New York, Buffalo, New York, United States and a 1-year NRC postdoctoral fellowship from the National Bureau of Standards. He joined NASA Goddard in 1980. He has worked on a number of astrophysics missions over the last 38 years, including Cosmic Background Explorer, ASTRO-E, ASTRO-E2 and ASTRO-H, Spitzer, WIRE, WISE, and James Webb Space Telescope. Currently, he is the subject matter expert for cryogenics on the XRISM/resolve x-ray microcalorimeter instrument.

**Megan E. Eckart** is a research scientist in the Astrophysics and Advanced Diagnostics Group at the Lawrence Livermore National Laboratory.

**Manuel Gonzalez** is a postdoc at the Astroparticle and Cosmology laboratory (APC), working on the design and characterization of low noise electronics for cryogenic detectors readout. He joined APC in 2020 after obtaining his PhD in physics at Balseiro Institute in Argentina. There, he worked on the microfabrication of III-V semiconductor heterostructures. He has experience in the design and deployment of scientific instruments, notably for the Pierre Auger Observatory and the QUBIC CMB experiment.

**Caroline A. Kilbourne** is a senior scientist at the X-ray Astrophysics Laboratory of NASA's Goddard Space Flight Center, where she's been developing low-temperature microcalorimeters for high-resolution x-ray spectroscopy since arriving as a post-doc in 1992. Her responsibilities at Goddard have ranged from advanced detector development at the sensor level to optimizing the myriad systems and their interfaces needed to progress from a promising sensor technology to a robust space-worthy spectrometer.

**Xiaoyi Li** is a payload/instrument systems engineer at NASA's Goddard Space Flight Center. She received her PhD from the University of Central Florida in 2005. She supported NASA missions since then, including Mars Science Laboratory, GLORY, RRM3, JWST, HIRMES, and Roman Space Telescope.

**Kazuhiro Sakai** is an assistant research scientist at the University of Maryland Baltimore County working at NASA Goddard Space Flight Center. He received his PhD in physics from the University of Tokyo in 2015 and was a postdoctoral researcher at the Institute of Space and Astronautical Science/Japan Aerospace Exploration Agency from 2015 until he became a postdoc at NASA GSFC in 2016.

**Damien Prêle** received his PhD from the Université Pierre et Marie Curie, in Paris, in 2007. He joined the Astroparticle Physics and Cosmology Laboratory immediately thereafter continuing his work in the field of cryogenic low noise instrumentation. Co-investigator for X-IFU Athena and Project Manager for the X-IFU Warm Front End Electronics since 2014, he develops low noise and low gain drift ASICs for the front-end electronics.

**Stephen J. Smith** is a research astrophysicist at NASA Goddard Space Flight Center. He received his MPhys degree in physics with space science and technology in 2002 and his PhD in physics in 2006, both from the University of Leicester, United Kingdom. He is an author of ~150 published papers. His primary research interests are in the development of cryogenic detectors and systems for x-ray astronomy applications.

**Nicholas A. Wakeham** is an assistant research scientist at the University of Maryland Baltimore County working at NASA Goddard Space Flight Center. He received his PhD in low temperature condensed matter physics from the University of Bristol in 2013 and was a postdoctoral researcher at Los Alamos National Laboratory from 2013 until he became a NASA Postdoctoral Fellow at GSFC in 2016. His interests are exotic electronic states, unconventional superconductivity, and superconducting detectors.

Biographies of the other authors are not available.